Eur. Phys. J. Special Topics **208**, 177–187 (2012)

DOI: 10.1140/epjst/e2012-01618-y

THE EUROPEAN PHYSICAL JOURNAL SPECIAL TOPICS

Regular Article

Depth-resolved magnetization distribution in ultra thin films by soft X-ray resonant magnetic reflectivity

J.-M. Tonnerre[1,a], E. Jal[1], E. Bontempi[2], N. Jaouen[3], M. Elzo[1,3], S. Grenier[1], H.L. Meyerheim[4], and M. Przybylski[4]

[1] Institut Néel, CNRS et Université Joseph Fourier, BP. 166, 38042 Grenoble Cedex 9, France
[2] Laboratorio di Chimica per le Tecnologie, Universita di Brescia, 25123 Brescia, Italy
[3] Synchrotron SOLEIL, L'Orme des Merisiers, Saint-Aubin, Boîte Postale 48, 91192 Gif-sur-Yvette Cedex, France
[4] Max-Planck-Institut für Mikrostrukturphysik, Weinberg 2, 06120 Halle, Germany

Received 21 December 2011 / Received in final form 23 March 2012
Published online 15 June 2012

Abstract. The analysis of complex magnetic profiles throughout an ultrathin magnetic films by soft X-ray resonant magnetic reflectivity is discussed. Subnanometer resolution can be achieved allowing the separation of interface and inner layer magnetic contributions as well as the determination of antiferromagnetic and non-collinear spin structures. Reflectivity measurements are carried out up to large scattering angles allowing the determination of the depth-resolved profiles of the out-of-plane magnetic component.

1 Introduction

In the late 80s, it has been shown that, in the vicinity of an absorption edge, the sensitivity to the magnetization of the X-ray scattering cross section can be resonantly enhanced and depends on the polarization state of the incident and scattered photons [1]. This effect results from electric multipole transitions which are sensitive to the magnetic properties of the system [2]. The first investigations were dedicated to bulk materials in the hard X-ray range, especially at the $L_{2,3}$ edges of rare earths and at the $M_{4,5}$ edges of actinides [3]. Later, strong effects have been observed in soft X-ray scattering measurements at the $L_{2,3}$ edges of $3d$ metals [4–6]. X-ray resonant magnetic scattering has been developed in third generation synchrotron radiation centers thanks to tunable polarized beam [7,8]. Used in various configurations, this technique, turned out to be a powerful tool for probing nanomagnetism [9]. In particular, by measuring the X-ray reflectivity, it is possible to probe the magnetic profile of a specific element across a thin magnetic film. Typically, X-ray resonant magnetic scattering is carried out by analyzing the energy dependence of the reflectivity at different incident angles or scattering vector values [10–14], whereas recently strong

[a] e-mail: jean-marc.tonnerre@grenoble.cnrs.fr

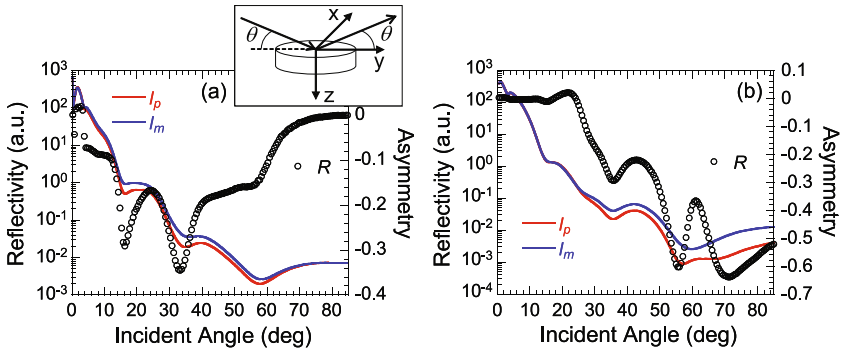

Fig. 1. Specular soft X-ray reflectivity and magnetic asymmetry measured at 705.9 eV for Au/Fe(4ML)/Cu(001) at room temperature in longitudinal configuration (a) and for Au/Fe(8ML)/Cu(001) at 40 K in polar configuration (b) (see text). Inset: sketch of the experimental geometry.

interest in the analysis of the angular dependence of the reflectivity has emerged [15–19]. This turns out to be particularly relevant in the soft X-ray range where the reflectivity, measured at large scattering angles, is sensitive to the out-of-plane magnetization [20]. Furthermore, soft X-ray resonant magnetic reflectivity (SXRMR) has been shown to resolve the magnetic structure along the growth axis with in-plane and perpendicular components [21].

2 Soft X-ray resonant magnetic reflectivity

X-ray resonant magnetic scattering exploits the magnetization sensitivity of the atomic scattering factor (ASF) at an absorption edge. Considering dipole transitions it may be expressed on the basis of the two polarization states chosen either parallel or perpendicular to the scattering plane [22]:

$$f = f_c \begin{pmatrix} 1 & 0 \\ 0 & \cos(2\theta) \end{pmatrix} - i f_m \begin{pmatrix} 0 & m_y \cos(\theta) + m_z \sin(\theta) \\ -m_y \cos(\theta) + m_z \sin(\theta) & -m_x \sin(2\theta) \end{pmatrix}. \tag{1}$$

The first term in Eq. (1) is the Thomson and resonant charge scattering with $f_c = f_0 + f'(E) + if''(E)$ where E is the incident photon energy. The second term is the resonant magnetic scattering where $f_m = m'(E) + im''(E)$ with m'' representing the X-ray magnetic circular dichroism (XMCD) [6]. The second terms in brackets show the contribution of the transverse (m_x), longitudinal (m_y) and polar (m_z) component of the magnetic moment to the scattering amplitude for a given experimental geometry. The scattering angle θ is defined as the angle between the incident beam direction and the sample surface (inset Fig. 1). In order to analyze the X-ray reflectivity measurements, it is usually convenient to consider the change of the refractive index or of the dielectric tensor at an interface and the propagation through a continuous layer. These complex quantities are related to the X-ray ASF for the forward scattering ($q = 0$) [23].

The magnetic properties of the $3d$ (transition metals) and $4f$ (rare earths) levels can be probed in the soft X-ray range (200 to 2000 eV) in the vicinity of their $L_{2,3}$ edges ($2p \rightarrow 3d$ transition) or $M_{4,5}$ edges ($3d \rightarrow 4f$ transition). These transitions exhibit sharp and strong resonances [24,25]. They provide a high charge and magnetic contrast allowing the study of multielement heterostructures. Furthermore, the

wavelength of soft X-rays is one order of magnitude larger than that of hard X-rays. The oscillations measured in reflectivity can then be observed to large incident angles which is favorable to probe the out-of-plane magnetic component.

The specular reflectivity measurements are performed under UHV conditions in order to both avoid absorption of the X-ray beam and to limit the surface contamination during measurements at low T. The in-plane magnetization is probed by applying a magnetic field in the sample plane either in the longitudinal (μ_0H in the scattering plane) or in the transverse geometry (μ_0H perpendicular to the scattering plane) using circular or linear (π) polarization of the incident beam [26,27]. The magnetic contrast in the reflectivity is derived from the measurement of two intensities Ip and Im, obtained either by using right and left circularly polarized incident light, keeping the direction of the applied magnetic field unchanged or measuring at remanence, or by reversing the direction of an applied magnetic field while keeping the X-ray helicity unchanged. The out-of-plane magnetization is probed by magnetizing the sample perpendicular to the sample plane (called here "polar" configuration). Up to now this condition has been realized by moving a permanent magnet close to the sample surface followed by data collection in remanence [20,21,28]. In this case, Ip and Im are obtained by reversing the X-ray helicity.

As an example, Fig. 1 displays spectra recorded in longitudinal and polar configuration using the RESOXS chamber [29] operated at the SIM beamline at the Swiss Light Source. Fig. 1(a) shows the measurements carried out at room temperature (RT) on a 4 monolayer (ML) thick Fe film deposited on a Cu(001) single crystal surface by pulsed laser deposition and capped by 3 nm of Au [12]. Solid lines represent the reflectivity curves Ip and Im collected in longitudinal geometry using a photon energy tuned close to the Fe L_3-edge and symbols represent the corresponding asymmetry defined by $R = [Ip - Im]/[Ip + Im]$. Figure 1(b) shows data collected at 40 K for a 8 ML Fe film which is known to exhibit an out-of-plane magnetic component [21]. The asymmetries observed for the different magnetization configurations (up to $\theta = 85$ degree) are completely different. In Fig. 1(a), R converges to zero at large θ values in agreement with the product $m_y \cos(\theta)$ in equation (1). By contrast, in Fig. 1(b), R adopts values significantly different to zero at high angles in agreement with the $m_z \sin(\theta)$ product. This allows the separation of the in- and out-of-plane component of the magnetization in an ultra-thin film [21] or in an exchange coupled layer [28].

In general the photon energy is tuned to the vicinity of the edge: either at the maximum of the XMCD contrast, which however is related to strong absorption, or at the inflexion point below and above the absorption edge to benefit from the strong contrast in the real magnetic part of the ASF and different signs of the resonant charge and magnetic terms.

The quantitative analysis of the magnetic structure is carried out by refining the energy and/or the angular dependent magnetic asymmetry at different incident angles or energies around the resonance, respectively. As an example, the Au/Fe(4ML)/Cu(001) sample introduced above is selected. The first requirement is to determine the energy dependent real and imaginary parts of the ASF. Ideally, the charge f'' and magnetic m'' imaginary parts should be obtained from X-ray absorption and XMCD spectra measured at the same time as the SXRMR experiment to benefit from the same energy resolution. However, these quantities are often derived from reference samples which might exhibit slightly different spectroscopic features. Moreover, the data are also usually collected at other beam lines involving a different energy resolution. Hence, the shape of the absorption and XMCD spectra can be slightly different. Since in a SXRMR experiment the magnetic contrast is linked to the magnetic moment via the result of the sum rules applied to the XMCD signal used [6], the differences can be a source of uncertainties in the determination of absolute magnetic moments. They do not affect the potential of SXRMR to determine

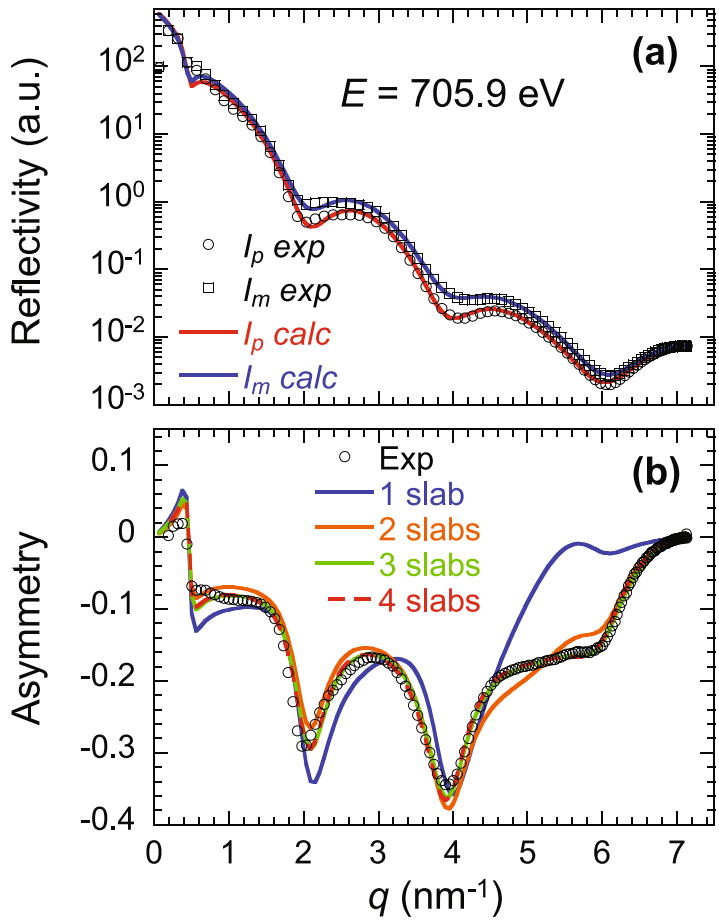

Fig. 2. Experimental and calculated reflectivity (a); experimental and calculated asymmetries (b) for Au/Fe(4ML)/Cu(001) at RT.

the film magnetization profile [20,28]. In the present study, f'' and m'' are determined from the measurements carried out on a reference Fe film, for which sum rules yield a magnetic moment of $2.1\mu_B$ [21]. The dispersive parts of the scattering amplitudes (f' and m') are calculated by using the Kramers-Kronig relationship.

The geometrical film structure is derived by fitting the reflectivity which is collected at energies far from resonance and/or by fitting the average signal $[Ip + Im]/2$ measured near the resonance. The latter is necessary to increase the charge contrast between the Fe layer and the Cu substrate. The following thickness and roughness parameters were obtained (in nm): $t_{\mathrm{Au}} = 3.0 \pm 0.02$, $t_{\mathrm{Fe}} = 0.93 \pm 0.10$; $\sigma_{\text{vac-Au}} = 0.23 \pm 0.02$, $\sigma_{\text{Au-Fe}} = 0.10 \pm 0.04$ and $\sigma_{\text{Fe-Cu}} = 0.33 \pm 0.02$. The film densities are refined to within 10% of the bulk values. The magnetic profile is then fitted while keeping the structure parameters constant.

Figure 2(a) shows the reflectivity Ip and Im collected in longitudinal geometry at 705.9 eV. Figure 2(b) exhibits the corresponding asymmetry and fits. Calculations are carried out by using a recursive calculation involving the reflection and transmission coefficients at each interface, within a magneto-optic formalism as described, for instance by Zak et al. [30] or by Elzo et al. [31]. The former formalism was coded in the early program "Reftool" [32], while the second was coded in the program "Dyna" [31]. Calculations shown here were performed with the Reftool program.

The Fe film is subdivided into thin slabs and the magnetization vector of each slab is described by an amplitude term (w_m, *where* $w_m = 1$ corresponds to a magnetic moment of $2.1\mu_B$) and two angles (spherical coordinates) to take into account arbitrary orientations of the magnetization vector. In the case of the 4 ML thick in-plane ferromagnetically ordered Fe sample, which was magnetized along the longitudinal direction, only the magnetic amplitude of each slab is refined by varying the weighting factors w_m applied to m' and m''. The fits are outlined in the following [see Fig. 2(b)]. Considering only one slab (blue solid line) or two equally thick slabs (light blue solid line) is insufficient to describe the magnetic structure. A very good agreement is obtained by using three equally thick slabs with, from the top to the bottom, $w_m = 1.07$, 0.42, 0.33 (green solid line). No further improvements are obtained at 705.9 eV using a four slabs model (red solid line). It is important to verify that the model which fits R also fits Ip and Im as shown in Fig. 2(a). It should be emphasized that the measurement of R at several energies around the resonance imposes a strong constraint to the analysis if the magnetic profile model is fitted to the whole data set [21]. In this example, the best model to fit R at several energies uses four slabs. The spatial resolution is equal to about 0.3 nm.

3 Applications of soft X-ray resonant magnetic reflectivity

In this section, two examples are discussed to illustrate the sensitivity of SXRMR to subtle details of magnetic film structures with in-plane and out-of-plane magnetic anisotropy.

3.1 Selective in-plane magnetization profile in $\mathbf{Ir/Fe_xMn_{1-x}/Ir}$

The first example outlines the investigation of single Fe_xMn_{1-x} magnetic alloy films epitaxially grown on an Ir(001) buffer layer and capped by Ir to protect the magnetic film from oxidation. It has been shown that for a [Fe_xMn_{1-x}/Ir] superlattice with x $\geq$ 0.7, the average magnetization depends on the c/a ratio which in turn depends on the concentration (x) [33]. Here, the aim is to investigate the homogeneity of the magnetic distribution within the layer to probe the potential effect of a strain and concentration distribution on the magnetization profile [34].

We first consider the analysis of the Fe and Mn magnetic profile in a 2.4 nm thick $Fe_{0.7}Mn_{0.3}$ film. The actual structural parameters of the film are derived from the refinement of hard X-ray reflectivity experiments. The SXRMR measurements were performed at RT using circularly polarized light and reversing the longitudinally applied magnetic field. The resonant terms of the ASF were derived from a bulk like Fe film (section 2) and an 1 ML Mn film deposited on Fe(001) ($w_m = 1$ corresponds to a magnetic moment of $3\mu_B$) [33]. The average magnetization of Fe in the alloy layer can be determined from energy dependent reflectivity measurements collected at small incident angle ($\theta = 5$ deg) where the reflectivity is less sensitive to the details of the charge density and magnetization profile [35]. Figure 3(a) and 3(b) shows the experimental reflectivity curves and the magnetic asymmetry. Considering only one slab (i.e. a uniform profile), the refinement of the asymmetry leads to a very good agreement between experiment and calculation (Fig. 3(b)). The corresponding calculated Ip and Im are displayed in Fig. 3(a). An average Fe magnetic moment of $0.65 \pm 0.05\,\mu_B$ per atom is derived, which is considerably lower than $2.1\,\mu_B$ for bcc-Fe. Figure 3(c) shows the experimental reflectivity curves and the asymmetry measured at $\theta = 17.5$ deg. A good fit is obtained for a homogenous magnetization (solid blue line), corresponding to an average Fe magnetic moment of $1.45 \pm 0.05\,\mu_B$. In the case

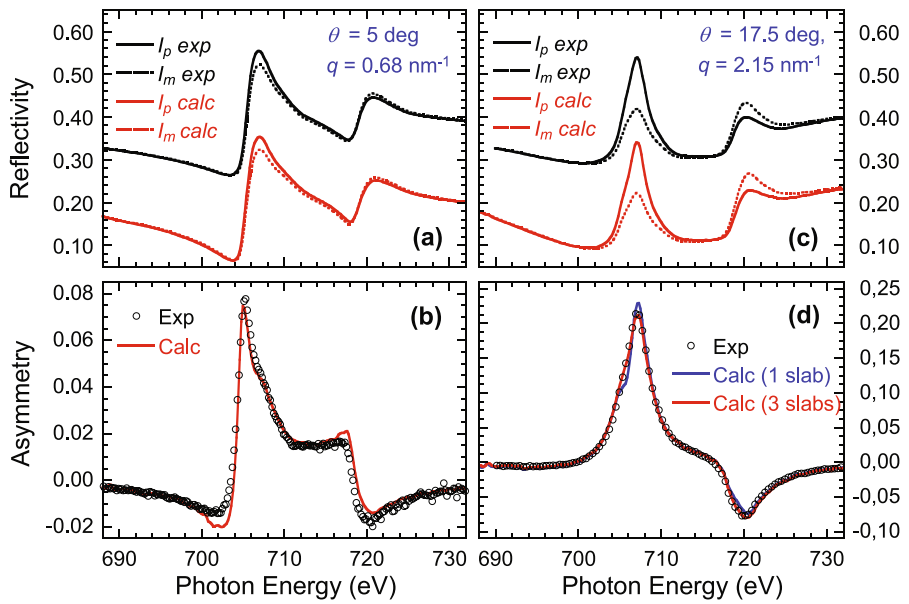

Fig. 3. Experimental and calculated energy dependent reflectivity measured at the Fe $L_{2,3}$ edge using the longitudinal configuration for Ir/$Fe_{0.7}Mn_{0.3}$/Ir(001) at 5 deg (a) and 17.5 deg (c) and corresponding asymmetry at 5 deg (b) and 17.5 deg (d).

of a uniform profile across the layer, the same magnetization amplitude is expected. However, at $\theta = 17.5$ deg, the measurements are more sensitive to the details of the magnetization profile. Hence, the observation of a large difference is an indication of a non uniform profile.

In order to probe the Fe magnetization profile within the film, the q dependent asymmetry has been recorded at 705.4 eV. Figure 4(a) displays the results. The solid blue line corresponds to a homogeneous film magnetization and fails to fit the experimental data, especially at high q values. Considering that the magnitude of the magnetic moment might be different depending on whether a magnetic atom is located at an interface or in the bulk of the film, the magnetic layer is divided into three slabs. The best fit (solid red line) refining six parameters (thickness and magnetic amplitude) yields the following values from the bottom to the top interface (given in nm and μ_B): 0.14, 0.08 / 1.54, 0.74 / 0.68, 0.48 (Fig. 4(c)). The average Fe magnetic moment derived from this model equals to 0.62 μ_B in good agreement with the one obtained from the energy dependent reflectivity analysis at 5 deg considering only one slab. Moreover, this three slabs magnetic profile allows not only the fit of R at $\theta = 5$ deg (not shown) but also at $\theta = 17.5$ deg (Fig. 3(d)). This confirms that the two different magnetic amplitudes, derived from the fit of the energy dependent asymmetry measured for two different incident angles, can be ascribed to a non uniform profile.

The magnetization profile is characterized by: (i) a net magnetic moment of 0.74 μ_B for the inner layer, (ii) a strongly reduced one at the bottom interface (0.08 μ_B) which is limited to about 1 ML (the d spacing of $Fe_{0.7}Mn_{0.3}$ is 0.165 nm) and (iii) an intermediate one (0.48 μ_B corresponding to a 35% reduction with respect to the magnetization of the inner part) at the top interface spread over 4 ML. Reversing the distribution of the magnetic moments within the film leads to a very different asymmetry ruling out such a model (solid green line).

In order to probe the Mn magnetic profile, the reflectivity measurements were carried out at 637.8 eV. Figure 4(b) shows that the asymmetry at the Mn L-edge

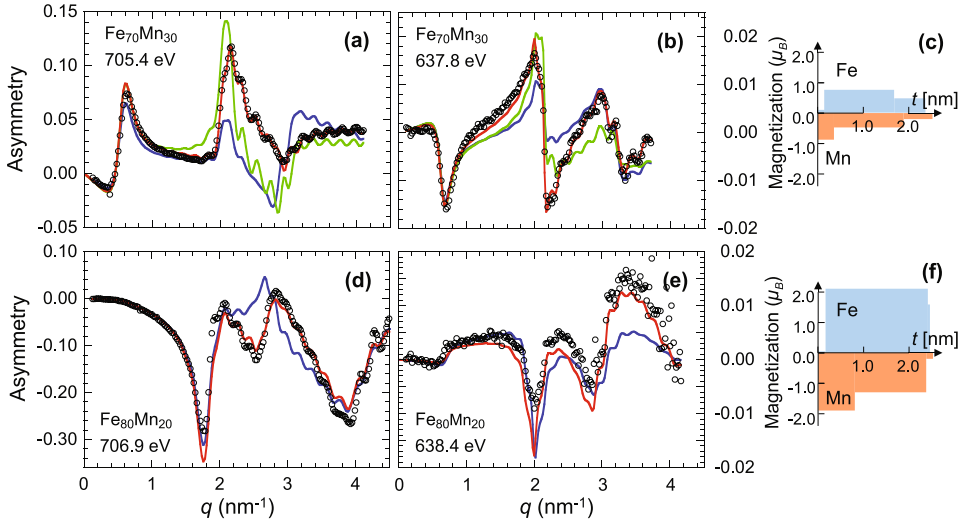

Fig. 4. Experimental (symbols) and calculated (solid lines, see text) angular dependent asymmetry measured for Ir/$Fe_{0.7}Mn_{0.3}$/Ir(001) at Fe (a) and Mn (b) L_3 edge using the longitudinal configuration. The same for Ir/$Fe_{0.8}Mn_{0.2}$/Ir(001) at Fe (d) and Mn (e) L_3 edge using the transverse configuration. On the right, sketches of the magnetic profile for $Fe_{0.7}Mn_{0.3}$ (c) and $Fe_{0.8}Mn_{0.2}$ (f) alloy thin films.

is weaker as compared to that at the Fe L-edge (2% versus 12%). Again a homogeneous distribution of the Mn magnetization can be ruled out on the basis of the large difference between the calculated (solid blue line) and the experimental asymmetry. Nevertheless, from the good agreement up to $1\,\mathrm{nm}^{-1}$, the average magnetic moment is derived to $-0.44\,\mu_B$. The negative sign indicates that the magnetic moment is oriented opposite to that of Fe, corresponding to an antiferromagnetic coupling between Fe and Mn. The best fit (solid red line) corresponds to the following parameters (in nm and μ_B): 0.35, $-0.87/1.53$, $-0.48/0.63$, -0.2 (Fig. 4(e)), with an average magnetic moment of $-0.46\,\mu_B$. The magnetic profile is graded. The magnetic moment decreases from the bottom to the top of the film. The differences between the Mn and the Fe magnetic profile are significant (no Mn "dead" layer) since the Mn asymmetry cannot be fitted with a Mn magnetization profile reproducing the shape of the Fe one (solid green line in Fig. 4(b)).

A similar trilayer with an alloy thin film of slightly different composition $Fe_{0.8}Mn_{0.2}$ was also investigated (Fig. 4(d)–4(f)). In this case, the SXRMR measurements were carried out at RT using π polarization and reversing the transversally applied magnetic field at a photon energy of 706.9 eV (Fe L_3 edge) and 638.4 eV (Mn L_3 edge). The analysis of the asymmetry rules out a constant magnetic distribution (solid blue line) and leads to similar magnetic profile as for $Fe_{0.7}Mn_{0.3}$ displayed in Fig. 4f (Fe: 0.17, 0.04 / 2.24, 2.1 / 0.05, 1.6 and Mn: 0.79, $-1.9/1.57$, $-1.3/0.15$, -0.2) with however a more homogeneous Fe magnetization and a larger average magnetic amplitude for Fe and Mn ($1.95\,\mu_B$ and $1.4\,\mu_B$, respectively). These values are closer to the $2.1\,\mu_B$ and $1.7\,\mu_B$, reported in [33] for $Fe_{0.9}Mn_{0.1}$.

The reduction of the average Fe and Mn magnetization, from $x = 0.8$ to $x = 0.7$, is linked to the increase of the tetragonal distortion induced by the Ir substrate [33]. The difference between the Mn and the Fe magnetic profile can be discussed in view of two effects. The first effect is the segregation of Mn atoms during the growth of the alloy as reported previously for a $Fe_{0.7}Mn_{0.3}$ thin film alloy by using high-resolution transmission-electron microscopy and electron-energy loss spectroscopy [34]. The

second one is the antiferromagnetic exchange interaction between Mn atoms. It is worth to note that SXRMR is not directly related to the magnetization but to the product of the magnetization with the concentration [10]. Hence, a change in the apparent magnetization could have its origin in a change of the concentration, not easily detectable by X-ray reflectivity on a 2.4 nm thick film. During growth, the segregation effect can lead to a non-homogeneous composition profile. The strong reduction of the Mn magnetic moment for the upper layers (concentrated on about the last atomic layer for $x = 0.8$ and spread over 4 ML for $x = 0.7$) can be related to a higher Mn concentration. The presence of Mn atoms surrounded by several Mn nearest neighbors may lead to an antiferromagnetic arrangement of the Mn magnetic moments and hence to a reduction of the laterally averaged magnetization. As a result, the Fe concentration is reduced and the Fe magnetization shows a decrease by 25% in the last atomic layer for $x = 0.8$ and by 35% in the last four layers for $x = 0.7$. This reduction might have its origin in a reduction of the Fe-Fe interactions or in a small change in the strain leading to a change of the Fe atomic volume [33]. In the interior of the film the composition is close to the nominal one and the amplitude of the magnetization is constant over about 9 to 10 ML. Close to the bottom interface, the Mn concentration might be slightly reduced, which might explain a more or less extended area with a higher Mn magnetization. Indeed, we observed an increase in the average magnetization from 0.46 to 1.4 μ_B value when the nominal Mn concentration is reduced from 0.3 to 0.2. Finally, the Fe "dead layer" could be ascribed to a first layer of almost pure Fe, however intermixed with Ir.

3.2 Out-of-plane magnetic profile in Fe(8ML) on Cu(001)

The face centered cubic (fcc) phase of Fe is notorious for its complex magnetic properties, both in the bulk and in the ultra thin film limit [36]. Although it is known since decades that fcc-Fe can be stabilized when deposited on Cu(001) a clear picture of its magnetic structure has not been established yet. Though some consensus exists that fcc-Fe films in the thickness range above 4 ML are not ferromagnetic (FM), their detailed magnetic structure is disputed. This called for a direct analysis of the magnetization profile in ultra-thin fcc-Fe by determining the depth-resolved magnetization profile [21] which has not been possible so far, especially for out-of-plane component, by conventional methods (except of Mossbauer spectroscopy, however Fe-^{57}Fe self-diffusion complicates interpretation in this case).

Here, we focus on the complex out-of-plane magnetic structure of the 8 ML sample introduced in Sect. 2. The structural parameters are derived from the refinement of the reflectivity curves collected in the hard X-ray range as well as in the vicinity of the Fe L_3 edge. Figure 5 shows the analysis of the asymmetry recorded at 40K for 2 photon energies at Fe L_3 edge. The high quality fits correspond to the magnetic structure ↑↑↓↑↓↑↓↑ where the upper 2 layers are FM coupled and the subsequent layers show an antiferromagnetic coupling [21].

The determination of the magnetic profile requires simultaneous refinement of several parameters. We followed the procedure described in Sect. 2 and limited the w_m amplitude to vary between 0 and 1.35 (which corresponds to the value for the high spin phase of fcc Fe 2.8 μ_B). It turns out that the main features of the experimentally derived asymmetry cannot be fitted by using less than six slabs. The best model to fit R at all photon energies (three at the L_3 edges and one at the L_2 one) is obtained using eight slabs and is shown on the right side of Fig. 5 (red), which is supported by DFT calculations [37].

In order to show the high sensitivity of R to the magnetic arrangement, the asymmetry was calculated for three other models (Fig. 5). The model consisting of

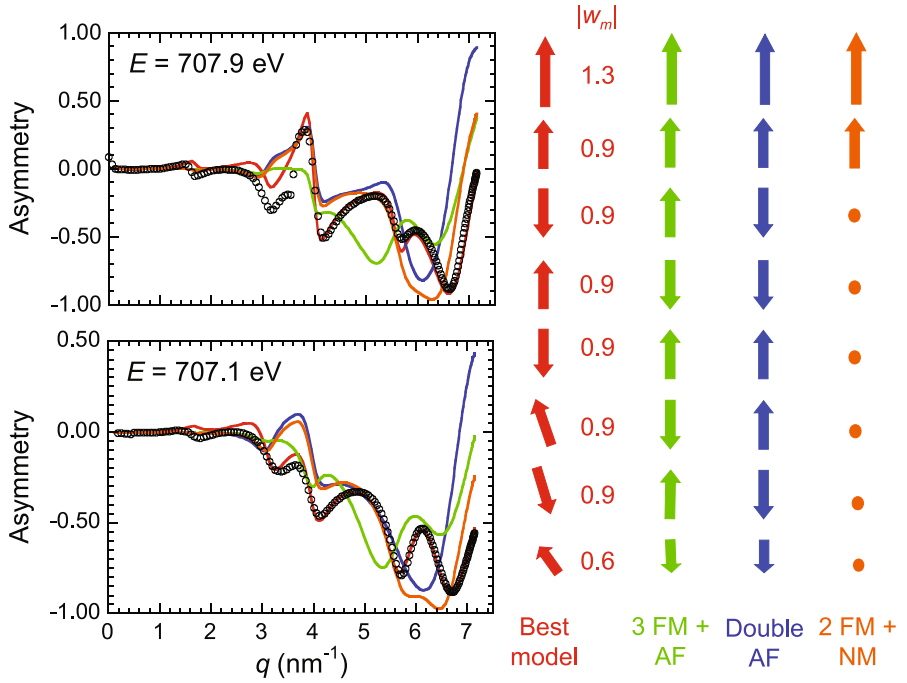

Fig. 5. (Left panel) experimental at 40 K (open circles) and calculated using 8 slices (solid lines) asymmetries for Au/Fe(8ML)/Cu(001). (Right panel) magnetization profiles corresponding to the calculation with the same color code.

three top FM layers followed by an AF structure (green arrows) and the double AF structure model (blues arrows) were theoretically proposed [38]. The model, with a surface magnetic layer and non-magnetic inner layers (orange arrows) which is based on an early study [39], allows one to illustrate the importance of the magnetization of the inner layer although the average is close to zero. The magnetic amplitudes were chosen identical to the best model. The calculated asymmetries are very different (Fig. 5) allowing us to rule out those models.

Finally, its is worth to note that a slight improvement of the calculated R at low angles has been obtained by introducing a small in-plane component through the rotation of the magnetic moment close to the Fe/Cu interface. Without such an in-plane component, the asymmetry at low angles shows no structure. A finite modulation of R is observed instead in the case of the 8 ML film (see Fig. 5) and it is even larger in the case of a 6 ML film [21].

4 Conclusion

We have reported on the application of SXRMR to derive the magnetization profile in ultra thin films. Owing to the combination of spectroscopy and scattering, SXRMR is site and element specific and is capable to provide information on complex magnetic structures. SXRMR studies on ultrathin films were carried out over a large angular range with high signal to noise ratio. Depth resolved in-plane and out-of-plane magnetization profiles have been derived with sub-nanometer resolution, including the determination of magnetization inhomogeneities within a strained alloy film and the analysis of magnetic configurations characterized by an antiferromagnetic structure

along the growth axis. It is anticipated that SXRMR will be very useful to probe the modifications induced in an entire film or from an interface by the application of a current or a voltage [40].

Some of us (JMT, EB, NJ) would like to acknowledge H. Fischer and M. Piecuch for the collaboration on FeMn samples. JMT, EJ, SG, HLM and MP acknowledge U. Staub for the collaboration of the RESOXS chamber at the Swiss Light Source (SLS) and the SIM beam line staff. The work at SLS was supported by the European Commission under the 6th Framework Programme: Strengthening the European Research Area, Research Infrastructures. Contract no°: RII3-CT-2004-506008.

References

1. D. Gibbs, D.R. Harshman, E.D. Isaacs, D.B. McWhan, D. Mills, C. Vettier, Phys. Rev. Lett. **61**, 1241 (1988)
2. J.P. Hannon, G.T. Trammell, M. Blume, D. Gibbs, Phys. Rev. Lett. **61**, 1245 (1988)
3. D.B. Mac Whan, J. Synch. Rad. **1**, 83 (1994), and references therein
4. C. Kao, J.B. Hastings, E.D. Johnson, D.P. Siddons, G.C. Smith, G.A. Prinz, Phys. Rev. Lett. **65**, 373 (1990)
5. C.-C. Kao, C.T. Chen, E.D. Johnson, J.B. Hastings, H.J. Lin, G.H. Ho, G. Meigs, J.-M. Brot, S.L. Hulbert, Y.U. Idzerda, C. Vettier, Phys. Rev. B. **50**, 9599 (1994)
6. J.-M. Tonnerre, L. Sève, D. Raoux, G. Soullié, B. Rodmacq, P. Wolfers, Phys. Rev. Lett. **75**, 740 (1995)
7. J.-M. Tonnerre, in *Magnetism and Synchrotron Radiation*, Lectures Notes (Mittelwihr, 1996)
8. E. Beaurepaire, B. Carrière, J.-P. Kappler (eds.) (Les Éditions de Physique, 1997)
9. J.B. Kortright, G. Srajer, J.C. Lang, D. Haskel, in *Modern techniques for characterizing magnetic materials*, edited by Y. Zhu (Springer, 2005)
10. L. Sève, N. Jaouen, J.-M. Tonnerre, D. Raoux, F. Bartolomé, M. Arend, W. Felsch, A. Rogalev, J. Goulon, C. Gautier, J.-F. Bérar, Phys. Rev. B **60**, 9662 (1999)
11. M. Sacchi, A. Mirone, Phys. Rev. B. **57**, 8408 (1998)
12. J.W. Freeland, K.E. Gray, L. Ozyuzer, P. Berghuis, E. Badica, J. Kavich, H. Zheng, J.F. Mitchell, Nat. Mat. **4**, 62 (2005)
13. A. Bergmann, J. Grabis, A. Nefedov, K. Westerholt, H. Zabel, J. Phys. D **39**, 842 (2006)
14. S. Valencia, A. Gaupp, W. Gudat, L.I. Abad, L.I. Balcells, B. Martinez, J. App Phys. **104**, 023903 (2008)
15. J.W. Freeland, V. Chakarian, Y.U. Idzerda, S. Doherty, J.G. Zhu, J.-H. Park, C.-C. Kao, Appl. Phys. Lett. **71**, 276 (1997)
16. Y. Choi, D. Haskel, R.E. Camley, D.R. Lee, J.C. Lang, G. Srajer, J.S. Jiang, S.D. Bader, Phys. Rev. B **70**, 134420 (2004)
17. K.-S. Lee, D.-E. Jeong, S.-K. Kim, J.B. Kortright, J. Appl. Phys. **97**, 083519 (2005)
18. S. Roy, M.R. Fitzsimmons, S. Park, M. Dorn, O. Petracic, Igor V. Roshchin, Zhi-Pan Li, X. Batlle, R. Morales, A. Misra, X. Zhang, K. Chesnel, J.B. Kortright, S.K. Sinha, I.K. Schuller, Phys. Rev. Lett. **95**, 047201 (2005)
19. S. Brück, S. Macke, E. Goering, X. Ji, Q. Zhan, K.M. Krishnan, Phys. Rev. B **81**, 134414 (2010)
20. J.-M. Tonnerre, M. De Santis, S. Grenier, H.C.N. Tolentino, V. Langlais, E. Bontempi, M. Garcia-Fernandez, U. Staub, Phys. Rev. Lett. **100**, 157202 (2008)
21. H.L. Meyerheim, J.-M. Tonnerre, L. Sandratskii, H.C.N. Tolentino, M. Przybylski, Y. Gabi, F. Yildiz, X.L. Fu, E. Bontempi, S. Grenier, J. Kirschner, Phys. Rev. Lett. **103**, 267202 (2009)
22. J.P. Hill, D.F. McMorrow, Acta Crystallogr. Sect. A **52**, 236 (1996)
23. J.B. Kortright, S.-K. Kim, Phys. Rev. B **62**, 12216 (2000)

24. J. Stöhr, H.C. Siegmann, *Magnetism: From Fundamentals to Nanoscale Dynamics*, Springer Series in Solid State Sciences 152, (Springer, Heidelberg, 2006)
25. N. Jaouen, J.-M. Tonnerre, D. Raoux, M. Müenzenberg, W. Felsch, A. Rogalev, N. Brookes, H. Dürr, G. van der Laan, Acta Phys. Pol. B **34**, 1403 (2003)
26. H.-Ch. Mertins, D. Abramsohn, A. Gaupp, F. Schäfers, W. Gudat, O. Zaharko, H. Grimmer, P.M. Oppeneer, Phys. Rev. B **66**, 184404 (2002)
27. J.-S. Lee, E. Vescovo, D.A. Arena, C.-C. Kao, J.-M. Beaujour, A.D. Kent, H. Jang, J.-H. Park, J.-Y. Kim, Appl. Phys. Lett. **96**, 042507 (2010)
28. J.M. Tonnerre, M. Przybylski, M. Ragheb, F. Yildiz, H.C.N. Tolentino, L. Ortega, J. Kirschner, Phys. Rev. B **84**, 100407(R) (2011)
29. N. Jaouen, J.-M. Tonnerre, G. Kapoujian, P. Taunier, J.-P. Roux, D. Raoux, F. Sirotti, J. Synch. Rad. **11**, 353 (2004)
30. J. Zak, E.R. Moog, C. Liu, S.D. Bader, J. Magn. Mat. **43**, 6423 (1991)
31. M. Elzo, E. Jal, O. Bunau, S. Grenier, Y. Joly, A.Y. Ramos, H.C.N. Tolentino, J.M. Tonnerre, N. Jaouen, J. Magn. Magn. Mat. **324**, 105 (2012) and `http://neel.cnrs.fr/spip.php?rubrique591`
32. `http://dimgruppi.ing.unibs.it/chimica/Bontempi/Reftool/reftool.html`
33. A. Déchelette, J.-M. Tonnerre, M.-C. Saint Lager, F. Bartolomé, L. Sève, D. Raoux, H. Fischer, M. Piecuch, V. Chakarian, C.C. Kao, Phys. Rev. B **60**, 6636 (1999)
34. H. Ardhuin, K. Suenaga, M.J. Casanove, E. Snoeck, C. Colliex, H. Fischer, S. Andrieu, M. Piecuch, Phys. Rev. B **58**, 14135(1998)
35. J.-M. Tonnerre, N. Jaouen, E. Bontempi, D. Carbone, D. Babonneau, M. De Santis, H.C.N. Tolentino, S. Grenier, S. Garaudee, U Staub, J. Phys.: Conf. Ser. **211**, 012015 (2010)
36. C.A.F. Vaz, J.A.C. Bland, G. Lauhoff, Rep. Prog. Phys. **71**, 056501 (2008)
37. L.M. Sandratskii, Phys. Rev. B **81**, 064417 (2010)
38. B.Y. Yavorsky, P. Zahn, I. Mertig, Phys. Rev. B **70**, 014413 (2004)
39. J. Thomassen, F. May, B. Feldmann, M. Wuttig, H. Ibach, Phys. Rev. Lett. **69**, 3831 (1992)
40. T. Maruyama, Y. Shiota, T. Nozaki, K. Ohta, N. Toda, M. Mizuguchi, A.A. Tulapurkar, T. Shinjo, M. Shiraishi, S. Mizukami, Y. Ando, Y. Suzuki, Nat. Technology **4**, 158 (2009)